Title

Operando
Calorimetry Investigation of Particle Size Effects on Heat Generation in WadsleyâRoth ($W_{0.2}V_{0.8})_3O_7$-Based E...

Journal

ACS Applied Energy Materials, 6(3)

ISSN

2574-0962 2574-0962

Authors

Baek, Sun Woong
Wyckoff, Kira E
Robertson, Daniel D
et al.

Publication Date

2023-01-27

DOI

10.1021/acsaem.2c03150

Peer reviewed

Effect of Particle Size on Heat Generation Rates in Fast-Charging Wadsley-Roth Shear Phase $(W_{0.2}V_{0.8})_3O_7$

Sun Woong Baek[a], Kira E. Wyckoff[b], Daniel D. Robertson[c], Matevž Frajnkovič[a], Yucheng Zhou[a], Sarah H. Tolbert[c], Ram Seshadri[b,d], and Laurent Pilon[a,e,f,+]

[a]Mechanical and Aerospace Engineering Department, Henry Samueli School of Engineering and Applied Science, University of California, Los Angeles, CA 90095, USA

[b]Materials Department, and Materials Research Laboratory, University of California, Santa Barbara, CA 93106, USA

[c]Department of Chemistry and Biochemistry, University of California, Los Angeles, CA 93106, USA

[d]Department of Chemistry and Biochemistry, University of California, Santa Barbara, CA 93106, USA

[e]California NanoSystems Institute, University of California, Los Angeles, Los Angeles, CA 90095, USA

[f]Institute of the Environment and Sustainability, University of California, Los Angeles, Los Angeles, CA 90095, USA

[+]Corresponding Author: Phone: +1 (310)-206-5598, Fax: +1 (310)-206-2302

E-mail: pilon@seas.ucla.edu

April 12, 2022

Abstract

The Wadsley-Roth shear phase compound $(W_{0.2}V_{0.8})_3O_7$ is a promising fast-charging electrode material with abilities to maintain its capacity at high C-rates and engage in multielectron redox reactions resulting in high specific capacity. Here, freeze-drying and solid-state methods were used to synthesized nano-sized and micro-sized $(W_{0.2}V_{0.8})_3O_7$ particles, respectively. Cyclic voltammetry and galvanostatic cycling demonstrated that $(W_{0.2}V_{0.8})_3O_7$ nanoparticles synthesized by freeze-drying method have superior electrochemical performance compared to the microparticles synthesized by solid-state method. Entropic potential measurements confirmed that the nanoparticles suppressed phase transitions and underwent shorter two-phase coexistence region. *Operando* calorimetry measurements established that the heat generation rate increased at the $(W_{0.2}V_{0.8})_3O_7$ electrode upon lithiation due to increase in charge transfer resistance. In addition, the entropy change dominated the reversible heat generation rate at each electrode. Moreover, the time-averaged irreversible heat generation rate was smaller at the electrode made of nanoparticles which was less electrically resistive than that made of microparticles. Finally the contribution of enthalpy of mixing was smaller for $(W_{0.2}V_{0.8})_3O_7$ particles synthesized by freeze-drying method compare to that of solid-state method confirming that smaller particle size was kinetically more advantageous for lithium-ions to intercalate than the larger particle size.

1 Introduction

Since their initial commercialization in the 1990s, lithium-ion batteries (LIBs) have served as the dominant energy source for portable electronics and electric vehicles. In the past decades, significant progress has been made in the development of LIB electrode materials. Different crystallographic structures, such as layered rocksalt-derived lithium cobalt oxide ($LiCoO_2$) [1], olivine lithium iron phosphate ($LiFePO_4$) [2], and spinel lithium manganese oxide ($LiMn_2O_4$) [3] have been developed as electrode materials for commercial batteries. However, for these conventional crystallographic structure materials, fast-charging is often hindered because of highly anisotropic solid-state diffusivity as well as the notable ion-path tortuosity associated with the crystallographic structure [4]. Alternatively, Wadsley-Roth shear phase compounds have been proposed as electrode materials for fast-charging LIBs. The Wadsley-Roth shear phase compounds typically contain some combination of edge- and corner-shared octahedra creating open-tunnel-like regions where Li^+ ions can rapidly diffuse during lithiation and delithiation [5–7]. Furthermore, nuclear magnetic resonance (NMR), magnetism, and conductivity measurements demonstrated that Wadsley-Roth shear phase materials have low activation barriers favorable to fast lithium diffusion [8, 9]. Among materials with Wadsley-Roth crystallographic shear structure, tungsten vanadium oxide $(W_{0.2}V_{0.8})_3O_7$ is a promising fast-charging electrode material for its abilities to maintain its capacity at high C-rates and engage in multielectron redox reactions resulting in high specific capacity [10]. Moreover, vanadium is more abundant than niobium. Thus, vanadium-based $(W_{0.2}V_{0.8})_3O_7$ is an interesting alternative to niobium-based Wadsley-Roth shear phase materials [10].

In addition to the new crystallographic framework offered by Wadsley-Roth shear phase compounds, mesoscale and nanoscale structuring of their particle morphology can further enhance their fast-charging ability by decreasing Li-ion diffusion distances within the particles. In fact, previous study demonstrated that electrodes with nanoscale $(W_{0.2}V_{0.8})_3O_7$ particles have better rate capability than those made of the microscale particles of the same compounds [10]. Even though the conventional electrochemical characterization methods,

such as galvanostatic cycling and cyclic voltammetry can give insight about the cycling performances of the battery materials, those methods are not able to measure the electrical conductivity nor the thermodynamic properties. Therefore, alternative characterization techniques are desirable to further investigate and understand the physicochemical phenomena taking place in battery electrode during cycling. In fact, entropic potential measurements can shed light on the entropic changes as well as the structural changes upon phase transitions in the electrode materials. Moreover, our custom made *operando* calorimetry [14] is capable of directly measuring the instantaneous heat generation rate in each electrode of a battery cell during charging/discharging. Thus, the *operando* calorimetry measurements can provide insights into the different phenomena contributing to energy dissipation upon charging/discharging including resistive losses.

The present study aims to identify the entropic and calorimetric signatures of the different physicochemical phenomena taking place during charging/discharging at the $(W_{0.2}V_{0.8})_3O_7$ working electrode with different particle sizes. Potentiometric entropy and *operando* isothermal calorimetry measurements were combined with other electrochemical characterization technique as well *in situ* as X-ray diffraction (XRD) measurements to understand the structural changes in the $(W_{0.2}V_{0.8})_3O_7$ upon lithiation/delithiation. Furthermore, the instantaneous heat generation rate measurements at each electrodes during cycling were used to gain insight into the physicochemical phenomena responsible for energy dissipation in the form of heat.

2 Background

2.1 Entropic potential measurements

2.2 Calorimetry measurements

Many calorimetric measurement techniques, such as accelerating rate calorimetry [18, 19], differential scanning calorimetry [20, 21], and *operando* isothermal calorimetry [5, 22] have

been used to investigate heat generation associated with battery operation. These calorimetric measurements were used not only to develop battery thermal management systems to avoid thermal runaway [19] but also to understand chemical reactions and transport processes taking place in the battery during cycling [5, 22]. Isothermal calorimetry is particularly insightful to reveal the heat generation associated with electrical energy losses [5, 22]. Furthermore, our previous *operando* isothermal calorimetry studies with our custom-made calorimeter [14] have revealed thermal signatures associated with various physicochemical phenomena including resistive losses [5,23–26], ion adsorption/desorption [23–26], electrolyte decomposition [24, 27], overscreening effect [27, 28], ion intercalation [24], and insulator to metal transition [5]. In this study, *operando* isothermal calorimetery was used to measure the instantaneous heat generation rates at each electrode to investigate the effect of particle size on the heat generation

2.2.1 Instantaneous heat generation rate

The total instantaneous heat generation rate $\dot{Q}_T(x,T)$ (in W) measured with *operando* isothermal calorimetry can be divided into four parts including (i) Joule heating $\dot{Q}_J(x,T)$, (ii) reversible entropic heat generation $\dot{Q}_{rev}(x,T)$, (iii) enthalpy of mixing $\dot{Q}_{mix}(x,T)$, and (iv) heat generation due to side reactions $\dot{Q}_{sr}(x,T)$. Thus, $\dot{Q}_T(x,T)$ can be expressed as [5, 22, 29, 30],

$$\dot{Q}_T(x,T) = \dot{Q}_J(x,T) + \dot{Q}_{rev}(x,T) + \dot{Q}_{mix}(x,T) + \dot{Q}_{sr}(x,T) \tag{1}$$

where $\dot{Q}_T(x,T)$ is positive when the battery releases heat and negative when it absorbs heat.

Under isothermal condition, the exothermic Joule heating $\dot{Q}_J(x,T)$ associated with irreversible resistive losses can be written as [5, 22, 29, 30],

$$\dot{Q}_J(x,T) = I[V(x,T) - U^{avg}(x,T)]. \tag{2}$$

Here, I is the applied current and $U^{avg}(x,T)$ is the open circuit voltage evaluated at the volume-average concentration in the cell considering a single electrochemical reaction [31].

In other words, $U^{avg}(x,T)$ is "the potential to which the cell would relax if the current were interrupted [30]." In practice, $U^{avg}(x,T)$ can be measured using GITT at the same C-rate as that used for the calorimetric measurements. In addition, [$V(x,T)$ - $U^{avg}(x,T)$] is the so-called battery overpotential corresponding to the voltage drop due to internal resistance.

In addition, the reversible entropic heat generation rate $\dot{Q}_{rev}(x,T)$ associated with the changes in the entropy of the battery upon cycling can be expressed as [22, 29, 30]

$$\dot{Q}_{rev}(x,T) = IT\frac{\partial U^{avg}(x,T)}{\partial T}. \tag{3}$$

Under extremely small current, Li would be uniformly distributed within the cell. Thus, the operating voltage $V(x,T)$ would be equal to the open circuit voltage $U_{ocv}(x,T)$, i.e., $V(x,T)$=$U^{avg}(x,T)$=$U_{ocv}(x,T)$. Then, $\dot{Q}_J(x,T) \simeq 0$ and heat generation would be solely due to $\dot{Q}_{rev}(x,T)$ [32]. However, under high C-rates, $\dot{Q}_J(x,T)$ dominates [32] and Li concentration gradients form within the electrode due to diffusion limitation. The latter results in additional irreversible heat generation due to enthalpy of mixing [5, 22, 29, 30], as discussed later.

The enthalpy of mixing $\dot{Q}_{mix}(x,T)$ associated with ion concentration gradients caused by mass transfer resistance in the LIB can be expressed as [22, 29, 30]

$$\dot{Q}_{mix}(x,T) = -\int_{V_\infty}\sum_i[\bar{h}_i(x,T) - \bar{h}_i^{avg}(x,T)]\frac{\partial c_i}{\partial t}dV \tag{4}$$

where V_∞ is the volume of the cell, $\bar{h}_i(x,T)$ is the partial molar enthalpy of species i and the superscript "avg" refers to the partial molar enthalpy corresponding to the volume-averaged concentration, and c_i is the local concentration of species i. For LIBs, the enthalpy of mixing can be further divided into four different contributions associated with ionic concentration gradients (i) across the electrolyte due to mass transfer, (ii) across the electrode due to non-uniform current distribution, (iii) within vacancies, and (iv) within intercalated lithium ions in the electrode due to electrochemical reactions [31, 33]. In general, the concentration gradient of the intercalated lithium ions represents the largest contribution to the enthalpy of mixing of the electrode [30]. Conceptually, $\dot{Q}_{mix}(x,T)$ should vanish if Li^+ ion transport is infinitely fast.

Lastly, the heat generation due to side reactions $\dot{Q}_{sr}(x,T)$ can be expressed as [22,29,30]

$$\dot{Q}_{sr}(x,T) = -\sum_i \Delta H_i \dot{r}_i(t) \tag{5}$$

where ΔH_i is the enthalpy of reaction of chemical reaction i occurring at reaction rate $\dot{r}_i(t)$. Note that most studies on heat generation in LIBS have neglected $\dot{Q}_{sr}(x,T)$ [22, 29, 30]. In fact, the side reactions are avoided by operating the device in an appropriate potential range [34]. Also, the aging process of LIBs takes place at relatively slow rates [29]. Thus, the magnitude of $\dot{Q}_{sr}(x,T)$ is negligible compare to $\dot{Q}_J(x,T)$, $\dot{Q}_{rev}(x,T)$, and $\dot{Q}_{mix}(x,T)$ under normal operation [22].

2.2.2 Energy balance

The total thermal energy Q_T (in J) released during a cycle as well as the irreversible heat dissipated in the form of Joule heating Q_J and enthalpy of mixing Q_{mix} can be expressed as [22]

$$Q_i = \oint_{cycle} \dot{Q}_i(x,T)\mathrm{d}t \quad \text{with } i = \ T,\ J,\ rev \text{ or } mix \tag{6}$$

By definition, integrating the reversible heat generation rate $\dot{Q}_{rev}(x,T)$ with respect to time over an entire cycle should vanish, i.e., Q_{rev}=0.

On the other hand, the net electrical energy losses ΔE_e (in J) corresponds to the difference between the electrical energy provided during charging and that recovered during discharging. It is illustrated by the hysteric voltage $V(x,T)$ profile [5, 22]. and expressed as [22]

$$\Delta E_e = \oint_{cycle} V(x,T)\mathrm{d}q = \oint_{cycle} V(x,T) I \mathrm{d}t \tag{7}$$

where q is the charge transferred upon electrochemical reaction so that I=dq/dt. Based on energy conservation principle, the total thermal energy Q_T dissipated during a full cycle is equal to ΔE_e, i.e.,

$$\Delta E_e = Q_J + Q_{mix} = Q_T. \tag{8}$$

3 Materials and methods

3.1 Synthesis of $(W_{0.2}V_{0.8})_3O_7$ powder

The solid-state preparation of $(W_{0.2}V_{0.8})_3O_7$ microparticles followed the synthesis described in Ref. [10]. Briefly, the material was prepared by heating a stoichiometric mixture of precursor oxide powders WO_3, V_2O_5, and V_2O_3 to 700 °C for 24 hours in a sealed vitreous silica tube, back-filled with a partial pressure of argon. After annealing, the tube was water quenched to room temperature to obtain $(W_{0.2}V_{0.8})_3O_7$ microparticles.

In addition, $(W_{0.2}V_{0.8})_3O_7$ nanoparticles were prepared by a freeze-drying method. First, 200 mg of NH_4VO_3 and 105 mg of $(NH_4)_{10}(H_2W_{12}O_{42})$ were added to 4 mL of distilled water and heated while stirring until the solids were fully dissolved. The resulting yellow solution was added dropwise to liquid nitrogen. After the removal of the remaining liquid nitrogen, the frozen solution was subjected to vacuum (<100 mTorr) on a Schlenk line for 10 – 20 hours to remove water. The dried powder was calcined in flowing Ar in a tube furnace at 700 °C for one hour reached with a heat ramp of 30 °C/min. The furnace was then cooled down to room temperature. The synthesized nanoparticles were stored under inert atmosphere to prevent unwanted surface oxidation.

3.2 Electrode and device fabrication

The same procedure was used to fabricate electrodes from $(W_{0.2}V_{0.8})_3O_7$ powders synthesized by the solid-state or the freeze-drying methods described previously. First, the synthesized $(W_{0.2}V_{0.8})_3O_7$ powder was ball-milled using a vortex mixer (Genie, Vortex-Genine) for 20 minutes in a 2 cm^3 canister with SuperP (TIMCAL) and carbon nanotubes (CNT). Then, the mixture was combined with polyvinylidene fluoride (PVDF) dissolved in N-methyl-2-pyrrolidone (NMP) to form a slurry with mass ratio 8:0.5:0.5:1 of $(W_{0.2}V_{0.8})_3O_7$:Super P:CNT:PVDF. The slurry was thoroughly mixed using a vortex mixer (Genie, Vortex-Genine) for 30 minutes before casting. A doctor blade set to 250 μm was used to cast the slurry onto a copper foil current collector. The electrode was dried in the vacuum oven

at 110 °C overnight. Then, electrodes were punched into a 10 mm diameter disc with mass loading of active material of about 6.5 mg/cm^2.

All coin cells were fabricated in an Ar-filled glove box using 2032 SS casings (MTI parts). They consisted of $(W_{0.2}V_{0.8})_3O_7$ electrode with 1 M of $LiPF_6$ in EC:DMC 1:1 v/v (Sigma Aldrich) as the electrolyte, polished metallic lithium (Sigma Aldrich) ribbon as the counter electrode, and a 50 μm thick Celgard C380 polypropylene/polyethylene separator. Cyclic voltammetry, galvanostatic cycling, and potentiometric entropy measurements were performed on the coin cells using a high accuracy potentiostat (Biologic, VSP-300) in the voltage range of 1.0−3.0 V.

3.3 Potentiometric entropy measurements

The open circuit voltage $U_{ocv}(x,T)$ and the entropic potential $\partial U_{ocv}(x,T)/\partial T$ of the coin cells were measured as functions of lithium composition x using the potentiometric entropy measurement technique and the appartus described in Ref. [5]. The potentiometric entropy measurements procedure consists of imposing a series of constant current pulses each followed by a relaxation period. Here, the constant current pulse lasted 30 minutes with a C-rate of C/10. After each current pulse, the cells were allowed to relax for 90 minutes. During the relaxation period, the temperature of the coin cell was varied from 15 °C to 25 °C in 5 °C increments by imposing a step-like temperature profile using a thermoelectric cold plate (TE technology, CP-121). The temporal evaluation of the cell voltage was recorded with a high accuracy potentiostat (Biologic, VSP-300). Likewise, $U^{avg}(x,T)$ and $\partial U^{avg}(x,T)/\partial T$ were measured using the same procedure and relaxation time as that used for measuring $U_{ocv}(x,T)$, but with pulses corresponding to different C-rates. The duration of the current pulses also changed with C-rates. For instance, at C-rate of 1C, each current pulse lasted 3 minutes, while it lasted 2 minutes for C-rate of 2C, and 1 minute for 3C. Before imposing the next temperature step and recording $U_{ocv}(x,T)$ or $U^{avg}(x,T)$, two conditions needed to be satisfied to ensure that the cell had reached thermodynamic equilibrium namely (i) the temperature difference between the cold plate and the top of the coin cell was less than 0.1 °C,

and (ii) the time rate of change of the open circuit voltage $\partial U_{ocv}(x,T)/\partial t$ or $\partial U^{avg}(x,T)/\partial t$ was less than 5 mV/h.

3.4 *Operando* isothermal calorimetry

The instantaneous heat generation rates at the $(W_{0.2}V_{0.8})_3O_7$ and lithium metal electrodes were measured separately under galvanostatic cycling using a custom-made isothermal calorimeter described previously [14]. The calorimetric cell consisted of (i) a 1 x 1 cm^2 $(W_{0.2}V_{0.8})_3O_7$-based electrode, (ii) two 50 μm thick Celgard C380 polypropylene/polyethylene separator sheets, (iii) 1 M $LiPF_6$ in EC:DMC 1:1 v/v (Sigma Aldrich) as the electrolyte, and (iv) polished metallic lithium (Sigma Aldrich) as the counter electrode.

As discussed in Ref. [14], the heat generation rate $\dot{Q}_i(t)$ (in mW) at each electrode was equal to the heat transfer rate $q_i''(t)$ passing through the 1×1 cm^2 thermoelectric heat flux sensor (greenTEG, gSKIN-XP) placed in thermal contact with the back of each electrode such that [14],

$$\dot{Q}_i(t) = q_i''(t)A_i = \frac{\Delta V_i(t)}{S_i}A_i \quad \text{with } i = WVO \text{ or } Li. \tag{9}$$

Here, ΔV_i is the voltage difference measured in each heat flux sensor, A_i denotes the footprint area of the electrode (in cm^2), and S_i is the temperature-dependent sensitivity of the heat flux sensor provided by the manufacturer (in $\mu V/(W/cm^2)$). The total instantaneous heat generation rate in the entire cell can be expressed as the sum of the heat generation rate measured at each electrode, i.e., $\dot{Q}_T(t) = \dot{Q}_{\mathrm{Li}}(t) + \dot{Q}_{\mathrm{WVO}}(t)$.

Moreover, the instantaneous heat generation rate $\dot{Q}_i(t)$ at electrode "i" can be divided into an irreversible $\dot{Q}_{irr,i}(t)$, and a reversible $\dot{Q}_{rev,i}(t)$ heat generation rate so that $\dot{Q}_i(t)$=$\dot{Q}_{irr,i}(t)$+$\dot{Q}_{rev,i}(t)$. Note that in battery electrode, $\dot{Q}_{irr,i}(t)$ depends on time as the electrical conductivity of the electrode may change upon lithiation/delithiation [5]. However, it is convenient to note that, time-averaging $\dot{Q}_{rev,i}(t)$ at each electrode over an entire cycle should yield zero. Thus, the time-averaged irreversible heat generation rate $\bar{\dot{Q}}_{irr,i}(t)$ at

electrode "i" can be expressed as

$$\bar{\dot{Q}}_{irr,i} = \frac{1}{t_c + t_d} \oint_{cycle} \dot{Q}_i(t)\mathrm{d}t \quad \text{with } i = \ WVO \text{ or } Li \tag{10}$$

where t_c and t_d are the duration of the charging (delithiation), and the discharging (lithiation) steps, respectively. The time-averaged heat generation rates during either the lithiation (subscript 'd") or the delithiation (subscript 'c") step can also be calculated as

$$\bar{\dot{Q}}_{i,j} = \frac{1}{t_j} \int_0^{t_j} \dot{Q}_i(t)\mathrm{d}t \quad \text{with } i = \ WVO \text{ or } Li \quad \text{and} \quad j = \ c \text{ or } d. \tag{11}$$

Thus, the time-averaged reversible heat generation rate during charging or discharging is given by

$$\bar{\dot{Q}}_{rev,i} = \bar{\dot{Q}}_{i,j} - \bar{\dot{Q}}_{irr,i} \quad \text{with } i = \ WVO \text{ or } Li \quad \text{and} \quad j = \ c \text{ or } d. \tag{12}$$

Furthermore, under galvanostatic cycling, the time t (in sec) can be converted into the lithium composition x in $\mathrm{Li}_x(\mathrm{W}_{0.2}\mathrm{V}_{0.8})_3\mathrm{O}_7$ such that

$$x = \frac{It}{3600MC_{theo}}. \tag{13}$$

Here, M is the mass loading of the active material and C_{theo} is the theoretical capacity of $(\mathrm{W}_{0.2}\mathrm{V}_{0.8})_3\mathrm{O}_7$ estimated as C_{theo}=230 mAh/g based on one electron per transition metal.

4 Results and discussion

4.1 Material and Electrochemical characterization

The sizes of the $(\mathrm{W}_{0.2}\mathrm{V}_{0.8})_3\mathrm{O}_7$ particles synthesized by solid-state or freeze-drying methods were characterized with FEI Apreo C scanning electron microscope (SEM) with a voltage of 15 kV and a current of 0.8 nA (Figure 1). First, both types of $(\mathrm{W}_{0.2}\mathrm{V}_{0.8})_3\mathrm{O}_7$ particles featured a rod-like morphology consistent with earlier transmission electron microscopy study [35]. Figure 1(a) shows the SEM image of $(\mathrm{W}_{0.2}\mathrm{V}_{0.8})_3\mathrm{O}_7$ microparticles synthesized by solid-state method. The average particle size was around 1-2 μm. On the other hand, the average length of the shorter side of the rod synthesized by freeze-drying method was about 100 nm.

[Figure 1(b)]. The smaller particle size of $(W_{0.2}V_{0.8})_3O_7$ could be originated from the shorter heating time discussed in the materials and method section.

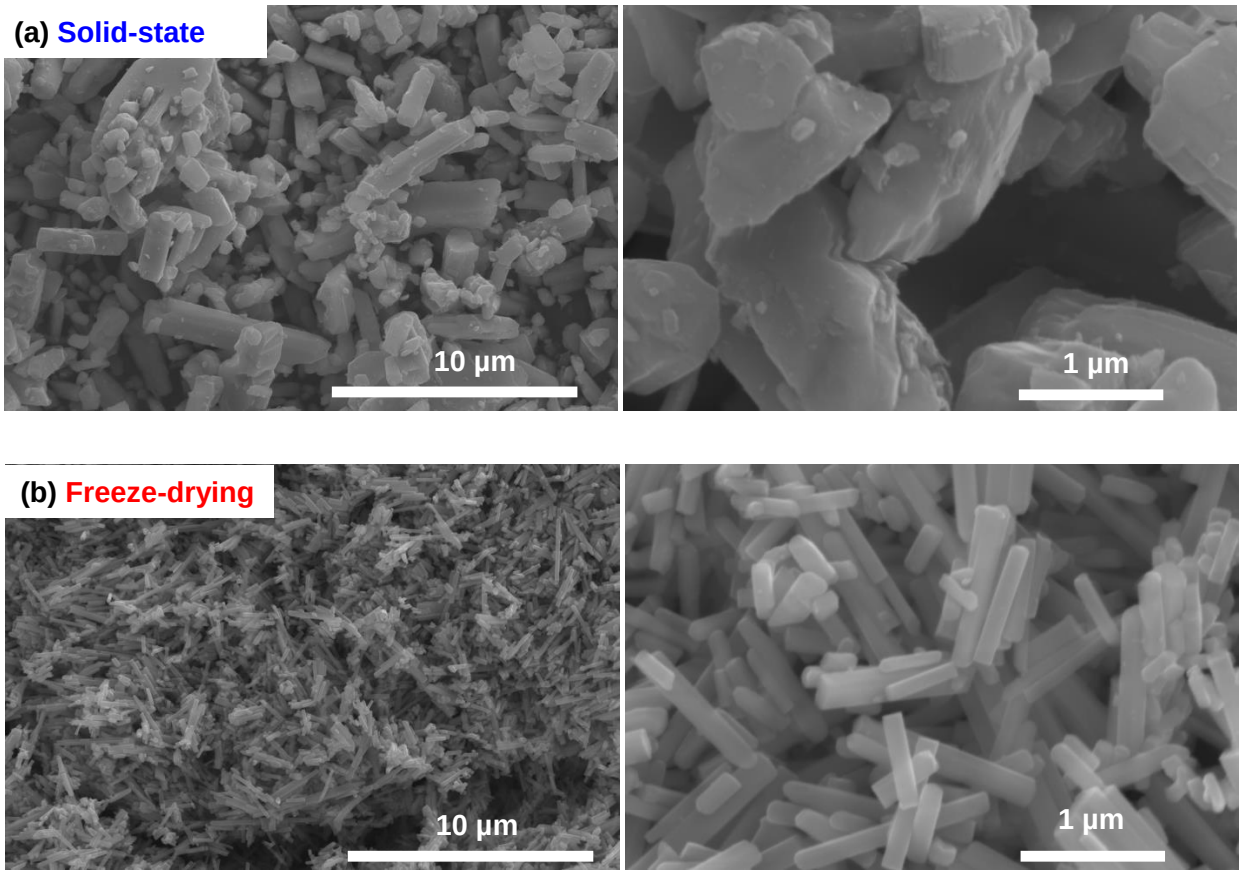

Figure 1: Scanning electron microscope image of $(W_{0.2}V_{0.8})_3O_7$ particles synthesized by (a) solid-state method, and (b) freeze-drying method.

The effects of particle size on the electrochemical behavior of coin cells were apparent in both cyclic voltammetry and galvanostatic cycling. Indeed, Figures 2(a) and 2(b) show cyclic voltammograms at different scan rates for potential window between 1.0 and 3.0 V vs. Li/Li^+ for electrodes made of $(W_{0.2}V_{0.8})_3O_7$ particles synthesized by solid-state and freeze-drying methods, respectively. Both $(W_{0.2}V_{0.8})_3O_7$-based electrodes showed redox peaks at similar potential at low scan rate ($\nu = 0.1$ mV/s). However, as scan rate increased, the redox peaks of electrode consisted of $(W_{0.2}V_{0.8})_3O_7$ microparticles synthesized by solid-state method shifted significantly compared to that of nanoparticles synthesized by freeze-drying

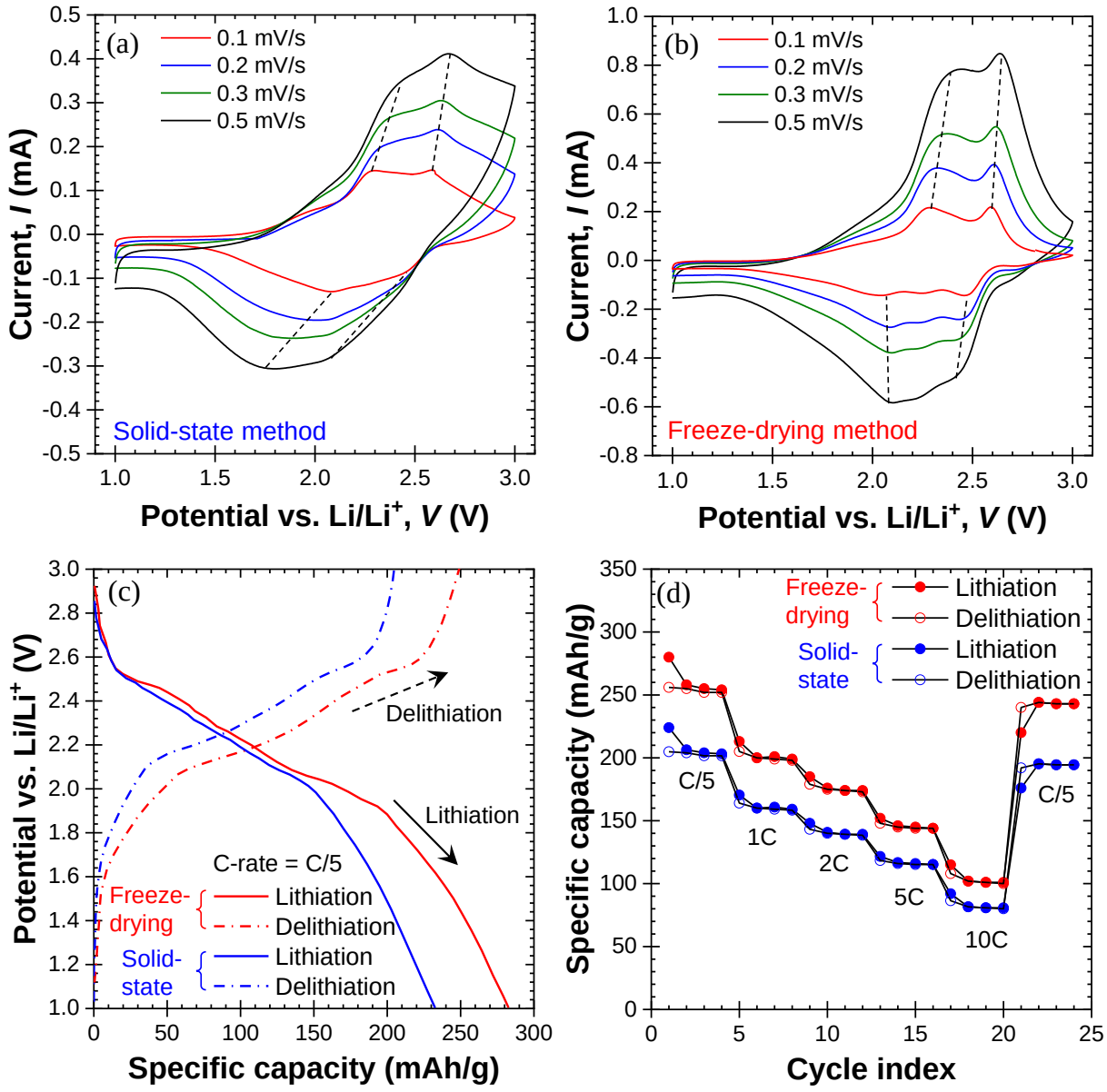

Figure 2: Cyclic voltammogram of half-cell containing electrode made of $(W_{0.2}V_{0.8})_3O_7$ particles synthesized by (a) solid-state method and (b) freeze-drying method cycled with potential window ranging from 1.0 to 3.0 V vs. Li/Li^+ at different scan rates ν, (c) galvanostatic charge-discharge potential profile at C-rate of C/5, and (d) specific capacity retention of the half-cell cycled between 1.0 and 3.0 V vs. Li/Li^+ at C-rates between C/5 and 10C.

method. This can be attributed to the fact that the redox reactions in the microparticles were kinetically more limited compared to the nanoparticles.

To further analyze the cyclic voltammetry, the b-values associated with each cathodic and anodic peak were obtained by fitting the peak current I_{peak} vs. scan rate ν with a power law such that $I_{peak} = a\nu^b$ (see Supplementary Material). Table 1 reports the b-values calculated for electrodes made of $(W_{0.2}V_{0.8})_3O_7$ microparticles synthesized by solid-state method and nanoparticles synthesized by freeze-drying method. The calculated b-values for all cathodic and anodic peaks for both electrodes were close to 0.5 suggesting that charging and discharging were limited by semi-infinite diffusion, and regardless of the particle size, $(W_{0.2}V_{0.8})_3O_7$ behaved as a battery-like material [36]. Furthermore, the calculated b-values of the electrode consisted of $(W_{0.2}V_{0.8})_3O_7$ nanoparticles were slightly larger than that of the microparticles suggesting that redox reactions in electrode with smaller particles were less kinetically limited [36].

Table 1: b-values for redox peaks of electrdoes made of $(W_{0.2}V_{0.8})_3O_7$ particles synthesized by solid-state and freeze-drying methods

Solid-state	**Oxidation**		**Reduction**	
Potential (V)	**2.08**	**2.46**	**2.26**	**2.58**
b-value	**0.57**	**0.52**	**0.55**	**0.56**
Freeze-drying	**Oxidation**		**Reduction**	
Potential (V)	**2.01**	**2.47**	**2.19**	**2.52**
b-value	**0.62**	**0.56**	**0.59**	**0.57**

Figure 2(c) shows the galvanostatic charge-discharge potential profile at C-rate of C/5 of half-cell containing electrodes composed of $(W_{0.2}V_{0.8})_3O_7$ particles synthesized by solid-state and freeze-drying methods between 1.0 and 3.0 V vs. Li/Li^+. The trends of voltage curves of both half-cells were almost identical during both lithiation and delithiation. However, specific capacity was measured to be 280 mAh/g for the half-cell with electrode made of $(W_{0.2}V_{0.8})_3O_7$ nanoparticles while 230 mAh/g for that of microparticles. Note that these

capacity values were higher than the theoretical capacity value calculated based on one electron per transition metal. Thus, these galvanostatic cycling data demonstrated the ability of $(W_{0.2}V_{0.8})_3O_7$ to engage in multielectron redox reaction also confirmed with X-ray photoelectron spectra measurements [10].

Furthermore, Figure 2(d) shows the specific capacity retention of half-cells with electrodes made of $(W_{0.2}V_{0.8})_3O_7$ microparticles and nanoparticles at different C-rates between C/5 and 10C at the same potential window. Again, half-cell containing electrode consisted of $(W_{0.2}V_{0.8})_3O_7$ nanoparticles cycled with higher capacity for all different C-rates compared to that of the $(W_{0.2}V_{0.8})_3O_7$ microparticles. Moreover, both electrodes showed impressive fast-charging ability. At C-rate of 10C, both maintained about 50 % of their specific capacity at C/5. In addition, after 20 cycles, they maintained their specific capacities and showed remarkable reversibility of $(W_{0.2}V_{0.8})_3O_7$ electrodes. Overall, galvanostatic cycling tests demonstrated the fast-charging ability of $(W_{0.2}V_{0.8})_3O_7$ as well as the performance advantage of nanoparticles synthesized by freeze-drying method in the cycling compared to the microparticles synthesized by solid-state method.

4.2 $U_{ocv}(x,T)$ and $\partial U_{ocv}(x,T)/\partial T$ measurements

To further understand the physicochemical phenomena occurring in those two different electrodes, open circuit voltage $U_{ocv}(x,T)$ and entropic potential $\partial U_{ocv}(x,T)/\partial T$ were measured for both electrodes consisted of $(W_{0.2}V_{0.8})_3O_7$ particles synthesized by freeze-drying and solid-state methods. Figure 3(a) plots the open circuit voltage $U_{ocv}(x,T)$ and entropic potential $\partial U_{ocv}(x,T)/\partial T$ of electrode consisted of $(W_{0.2}V_{0.8})_3O_7$ microparticles synthesized by solid-state method while Figure 3(b) plots those of $(W_{0.2}V_{0.8})_3O_7$ nanoparticles synthesized by freeze-drying method at 20 °C as functions of x composition in $Li_x(W_{0.2}V_{0.8})_3O_7$ at C-rate of C/10 during lithiation. The trends of both $U_{ocv}(x,T)$ and $\partial U_{ocv}(x,T)/\partial T$ of $(W_{0.2}V_{0.8})_3O_7$ particles synthesized by two different methods were very similar. However, the electrode made of $(W_{0.2}V_{0.8})_3O_7$ nanoparticles was able to accommodate more lithium and showed larger x composition compared to that of the microparticles as also observed

from the galvanostatic cycling.

Based on the slope of $U_{ocv}(x,T)$ and $\partial U_{ocv}(x,T)/\partial T$, three regions could be identified. In the first region, for $x < 1.5$ for the electrode made of $(W_{0.2}V_{0.8})_3O_7$ microparticles synthesized by solid-state method and for $x < 1.7$ for that of nanoparticles synthesized by freeze-drying method, $U_{ocv}(x,T)$ decreased linearly indicating lithium insertion in a homogeneous solid solution also confirmed with *in situ* XRD measurement [10]. However, in the same region, $\partial U_{ocv}(x,T)/\partial T$ increased first then decreased at higher x composition resulting in a local maxima. This behavior of $\partial U_{ocv}(x,T)/\partial T$ curves could be attributed to a sharp increase in the charge transfer resistance known to occur in this region observed with potentiostatic electrochemical impedance spectroscopy [10]. The charge transfer resistance of the electrode consisted of $(W_{0.2}V_{0.8})_3O_7$ nanoparticles was initially 30 Ω at $x = 0$ but it increased to 130 Ω at x= 0.6 upon lithiation [10]. After the initial sharp increase, the charge transfer resistance of $(W_{0.2}V_{0.8})_3O_7$ electrode stayed around the same value throughout all x composition [10]. Thus, the peak shape in $\partial U_{ocv}(x,T)/\partial T$ in the low lithium composition region could be attributed to the associated electronic entropy change due to sharp increase in charge transfer resistance. Furthermore, for $1.5 < x < 2.3$ for the electrode composed of microparticles and for $1.7 < x < 2.4$ for that of nanoparticles, both $U_{ocv}(x,T)$ and $\partial U_{ocv}(x,T)/\partial T$ were more or less constant confirming a two-phase coexistence region also observed previously in XRD measurements [10]. Interestingly, the two-phase coexistence region was observed to last shorter for the the electrode made of nanoparticles than that of microparticles. The two-phase coexistence region was observed to last about 0.8 lithium for microparticles while 0.7 lithium for nanoparticles. In fact, smaller particles, having shorter lithium-ion diffusion distances within the particle, often observed to suppress phase transitions [12, 13, 37]. In addition, for $x > 2.3$ for the electrode consisted of $(W_{0.2}V_{0.8})_3O_7$ microparticles and for $x >$ 2.4 for that of nanoparticles, both $U_{ocv}(x,T)$ and $\partial U_{ocv}(x,T)/\partial T$ decreased monotonically indicating lithium insertion in a homogeneous solid solution consistent with the observation from *in situ* XRD measurements [10]. Lastly, Figure 3(C) plots $\partial U_{ocv}(x,T)/\partial T$ of both electrode consisted of $(W_{0.2}V_{0.8})_3O_7$ particles synthesized by solid-state and freeze-drying

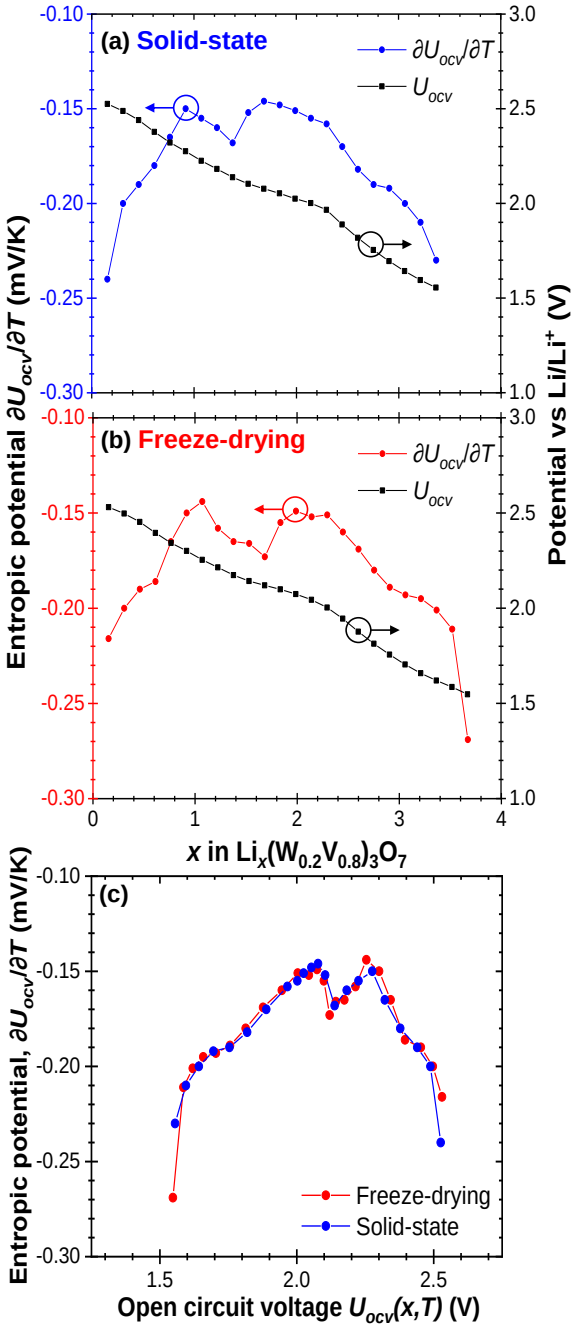

Figure 3: Open circuit voltage $U_{ocv}(x,T)$ and entropic potential $\partial U_{ocv}(x,T)/\partial T$ of the half-cell containing electrodes made of $(W_{0.2}V_{0.8})_3O_7$ particles synthesized by (a) solid-state and (b) freeze-drying methods as functions of lithium composition x in $Li_x(W_{0.2}V_{0.8})_3O_7$, (c) $\partial U_{ocv}(x,T)/\partial T$ of both half-cells as functions of $U_{ocv}(x,T)$. All data are for lithiation at temperature T = 20 °C.

methods as functions of $U_{ocv}(x,T)$. Note that $\partial U_{ocv}(x,T)/\partial T$ of two different electrodes were almost identical when they are plotted as functions of $U_{ocv}(x,T)$. Thus, it implies that the physicochemical phenomena occurring in the $(W_{0.2}V_{0.8})_3O_7$ did not change with different particle size.

4.3 Heat generation rates

4.3.1 Instantaneous heat generation rates

Figures 4(a)-4(c) plot the instantaneous heat generation rates $\dot{Q}_{WVO}$ measured at the electrode made of $(W_{0.2}V_{0.8})_3O_7$ microparticles synthesized by solid-state method and $\dot{Q}_{Li}$ at the lithium metal electrode as functions of dimensionless time t/t_{cd} with t_{cd} being the charging(delithiation)/ discharging(lithiation) cycle period, for three consecutive cycles at temperature of 20 °C, and at C-rate of 1C, 2C, 3C, respectively. Likewise, Figures 4(d)-4(f) plot $\dot{Q}_{WVO}$ measured at the electrode consisted of $(W_{0.2}V_{0.8})_3O_7$ nanoparticles synthesized by freeze-drying method and $\dot{Q}_{Li}$ at the lithium metal electrode as functions of dimensionless time t/t_{cd} at C-rate of 1C, 2C, 3C, respectively under the same condition. First, the measurements at each electrode were repeatable cycle after cycle. In addition, the trend of both $\dot{Q}_{WVO}$ for both electrodes made of $(W_{0.2}V_{0.8})_3O_7$ microparticles and nanoparticles were very similar. Here, the magnitude of both $\dot{Q}_{WVO}$ for microparticles and nanoparticles started very low since the pristine $(W_{0.2}V_{0.8})_3O_7$ particles were electrically conductive [10]. However, $\dot{Q}_{WVO}$ increased rapidly due to the increase in charge transfer resistance with increasing x composition in $Li_x(W_{0.2}V_{0.8})_3O_7$ upon discharging (lithiation) [10]. In addition, $\dot{Q}_{WVO}$ for electrode composed of $(W_{0.2}V_{0.8})_3O_7$ nanoparticles increased more of less linearly upon discharging while $\dot{Q}_{WVO}$ for electrode composed of $W_{0.2}V_{0.8})_3O_7$ microparticles featured small plateau-like region upon discharging. This could be attributed to the $(W_{0.2}V_{0.8})_3O_7$ nanoparticles synthesized by freeze-drying method suppressing two-phase coexistence region [12,13,37]. Moreover, the plateau-like region observed for electrode made of $W_{0.2}V_{0.8})_3O_7$ microparticles could also be enhanced by the reversible heat generation $\dot{Q}_{rev}$

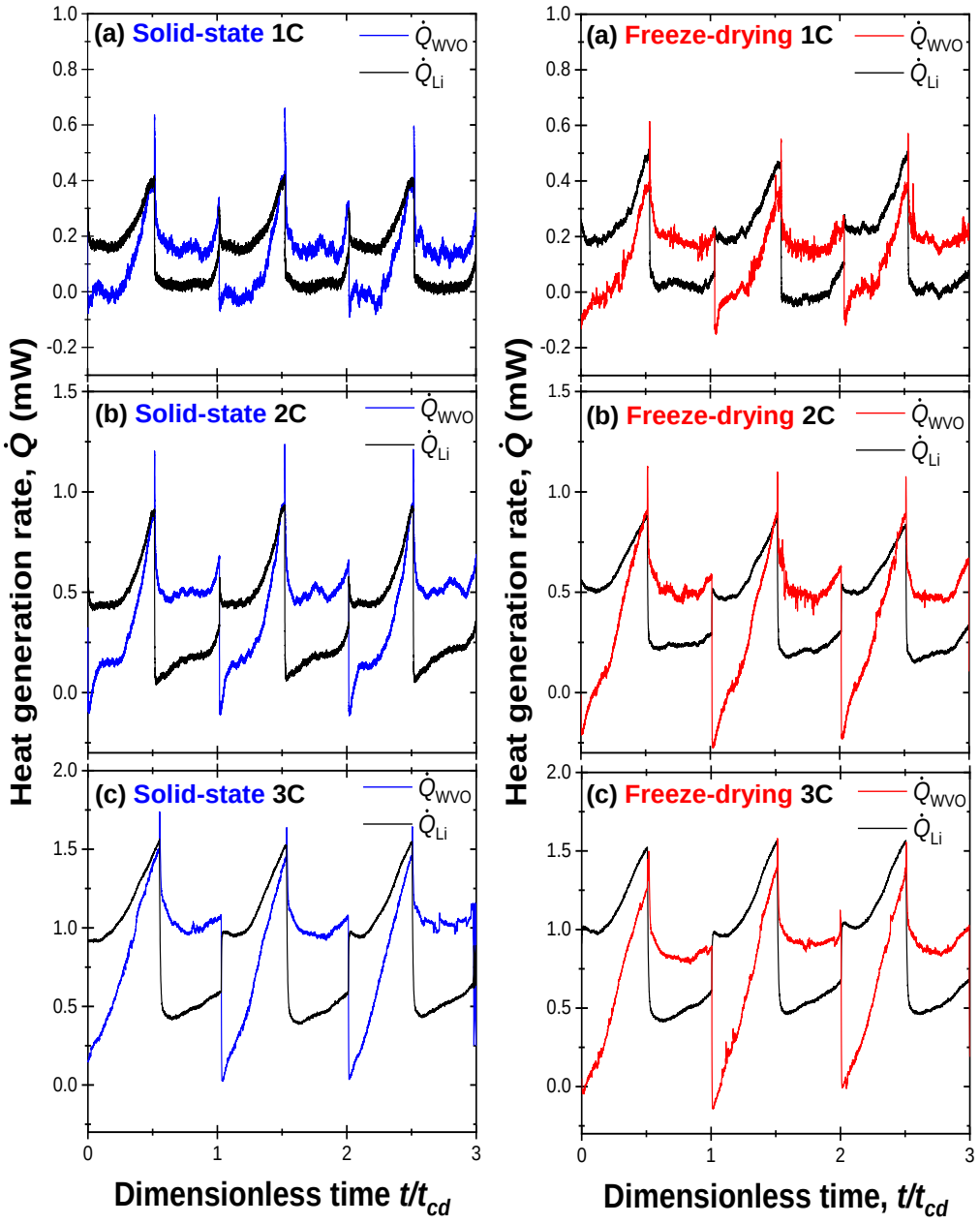

Figure 4: Measured instantaneous heat generation rates $\dot{Q}_{WVO}$ at the $(W_{0.2}V_{0.8})_3O_7$-based electrodes, $\dot{Q}_{Li}$ at the lithium metal electrode as functions of dimensionless time t/t_{cd} for three consecutive cycles with potential window ranging from 1.0 V to 3.0 V vs. Li/Li^+ at C-rates of (a) 1C, (b) 2C, and (c) 3C for $(W_{0.2}V_{0.8})_3O_7$ microparticles synthesized by solid-state method, and (d) 1C, (e) 2C, (f) 3C for $(W_{0.2}V_{0.8})_3O_7$ nanoparticles synthesized by freeze-drying methods.

[Eq.(5)] as observed from the entropic potential measurements [Figure 3(a)].

4.3.2 Time-averaged heat generation rates

To further investigate the effect of particle size on the heat generation, time-averaged irreversible heat generation rates $\bar{\dot{Q}}_{irr,WVO}$ and $\bar{\dot{Q}}_{irr,Li}$ were calculated [Eq.(11)]. In Figure 5(a), the square data points corresponds to the average of $\bar{\dot{Q}}_{irr,WVO}$ and $\bar{\dot{Q}}_{irr,Li}$ over 5 consecutive cycles, and the error bars represents two standard deviations or 95 % confidence interval. Fitting of $\bar{\dot{Q}}_{irr,Li}$ at the metallic Li electrode in a calorimetric cell with electrodes made of $(W_{0.2}V_{0.8})_3O_7$ particles synthesized by freeze-drying method and solid-state method indicates that it increased quadratically with respect to I, i.e., $\bar{\dot{Q}}_{irr,Li} \propto I^2$. In other words, the irreversible heat generation was dominated by Joule heating as the resistance of the metallic Li electrode was constant. Meanwhile, $\bar{\dot{Q}}_{irr,WVO}$ at the $(W_{0.2}V_{0.8})_3O_7$-based electrode containing microparticles synthesized by solid-state method was similar to that of the nanoparticles synthesized by freeze-drying method at C-rate of 1C corresponding to 1.5 mA for solid-state and 1.6 mA for freeze-drying methods. However, $\bar{\dot{Q}}_{irr,WVO}$ of the electrode composed of $(W_{0.2}V_{0.8})_3O_7$ microparticles became larger than that of the nanoparticles at C-rate of 2C and 3C even with smaller currents I. This effect could be attributed to the fact that an electrode with larger particles generally shows larger electrical resistivity thus increasing Joule heating [11]. In addition, enthalpy of mixing could also contribute to this behavior. Decreasing the particle size shortens the time required for lithium ion insertion into the host material, thereby decreasing the concentration gradients formed within the particles and decreasing the irreversible heat generation associated with enthalpy of mixing [Eq.(6)] [31,33]. Overall, $\bar{\dot{Q}}_{irr,WVO}$ of the electrode made of the smaller $(W_{0.2}V_{0.8})_3O_7$ particles synthesized by the freeze-drying method was smaller than that of the larger $(W_{0.2}V_{0.8})_3O_7$ particles synthesized by the solid-state method.

Furthermore, Figure 5(b) plots the absolute value of time-averaged reversible heat generation rate $|\bar{\dot{Q}}_{rev,WVO,j}|$ at the $(W_{0.2}V_{0.8})_3O_7$-based electrode consisted of $(W_{0.2}V_{0.8})_3O_7$ microparticles synthesized by solid-state method and nanoparticles synthesized by freeze-

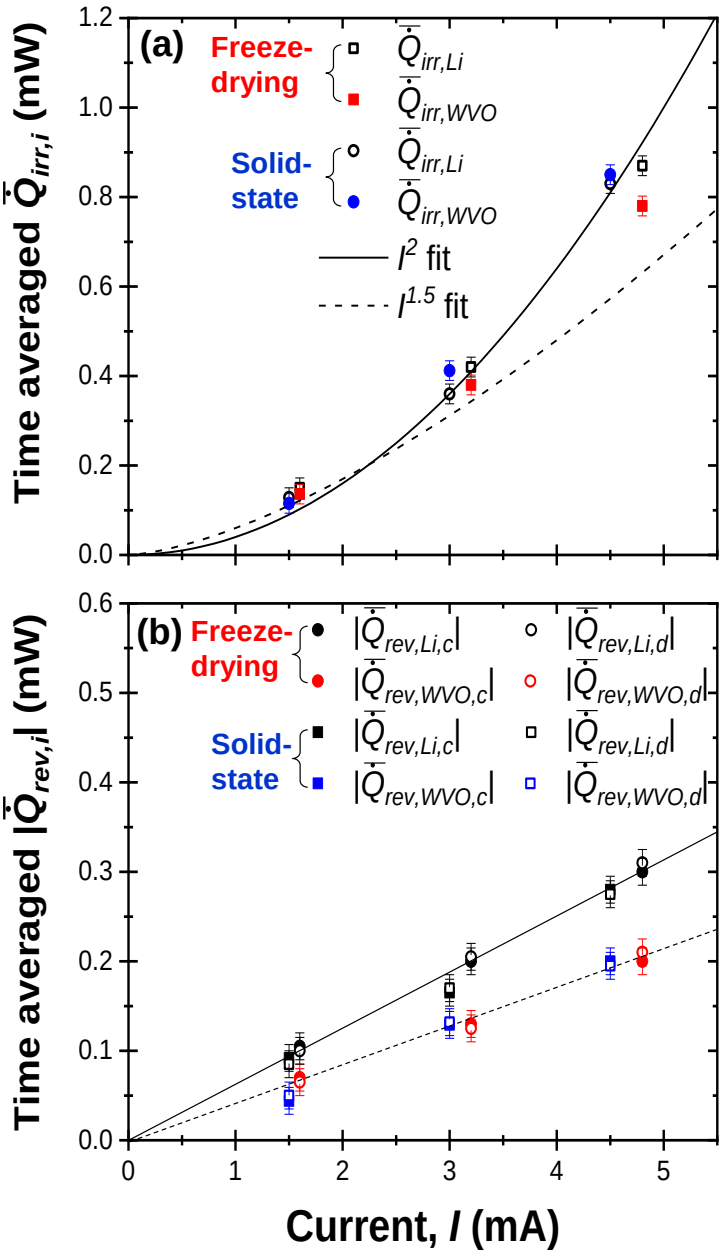

Figure 5: Time-averaged (a) irreversible heat generation rates $\bar{\dot{Q}}_{irr,WVO}$ and $\bar{\dot{Q}}_{irr,Li}$, and (b) reversible heat generation rates $|\bar{\dot{Q}}_{rev,WVO,j}|$ and $|\bar{\dot{Q}}_{rev,Li,j}|$ during charging ($j = c$) and discharging ($j = d$) as functions of applied current I, based on the isothermal *operando* calroimetry measurement at temperature $T = 20$ °C.

drying method, and $|\bar{\dot{Q}}_{rev,Li,j}|$ at the lithium metal counter electrode computed according to Eqs.(11)-(13) during lithiation (j=d) and delithiation (j=c) for different currents I. Here,

$\bar{\dot{Q}}_{rev,Li}$ was exothermic (> 0) during discharging (lithiation) and endothermic (< 0) during charging (delithiation) whereas $\bar{\dot{Q}}_{rev,WVO}$ was endothermic during discharging(lithiation) and exothermic during charging(lithiation). It establishes that both $|\bar{\dot{Q}}_{rev,WVO,j}|$ and $|\bar{\dot{Q}}_{rev,Li,j}|$ at each electrode were identical during lithiation and delithiation, confirming their reversible nature. Furthermore, both $|\bar{\dot{Q}}_{rev,WVO,j}|$ and $|\bar{\dot{Q}}_{rev,Li,j}|$ were linearly proportional to the current I. Interestingly, this effect could be attributed to the fact that the reversible heat generation rate was dominated by the entropy change. Since the entropic potential measurements of both electrodes made of $(W_{0.2}V_{0.8})_3O_7$ particles synthesized by freeze-drying and solid-state methods were almost identical, both $|\bar{\dot{Q}}_{rev,WVO}|$ at those electrodes also followed similar trend.

4.3.3 Heat generation rate of a full cell

Figures 6(a) and 6(b) plot the total instantaneous heat generation rate $\dot{Q}_T(x) = \dot{Q}_{Li}(x) + \dot{Q}_{WVO}(x)$ measured in the entire cell containing electrode made of $(W_{0.2}V_{0.8})_3O_7$ microparticles synthesized by solid-state method as a functions of lithium composition x in $Li_x(W_{0.2}V_{0.8})_3O_7$ at C-rate of 3C during lithiation and delithiation, repectively. Likewise, Figures 6(c) and 6(d) plot those for $(W_{0.2}V_{0.8})_3O_7$ nanoparticles synthesized by freeze-drying method during lithiation and delithiation, repectively. It also shows the contributions from Joule heating $\dot{Q}_J(x)$ as well as the reversible heat generation $\dot{Q}_{rev}(x)$, respectively calculated based on Eqs.(4) and (5) [5,22,29,30]. Here, $\dot{Q}_{rev}(x)$ was exothermic during lithiation and endothermic during delithiation as expected from the sign of $\partial U_{ocv}(x,T)/\partial T$ shown in Figures 3(a) and 3(b). Moreover, the trend of the calculated sum $\dot{Q}_J(x) + \dot{Q}_{rev}(x)$ agreed relatively well with the measured total heat generation rate $\dot{Q}_T$ for both lithiation and delithiation. However, there were still some deviations between the calculated sum $\dot{Q}_J(x) + \dot{Q}_{rev}(x)$ and measured $\dot{Q}_T(x)$. Neglecting the heat generation rate due to side reaction $\dot{Q}_{sr}(x)$, the difference was attributed to the enthalpy of mixing $\dot{Q}_{mix}$, i.e., $\dot{Q}_{mix}(x) = \dot{Q}_T(x)$ - $\dot{Q}_J(x)$ - $\dot{Q}_{rev}(x)$ [Eq.(8)]. In general, the effect of $\dot{Q}_{mix}(x)$ increased with increasing C-rates due to larger lithium concentration gradients developed within the electrode due to the diffusion limita-

tion [31, 33]. However, calculating the enthalpy of mixing $\dot{Q}_{mix}(x)$ as a function of lithium composition x is rendered difficult by the fact that it not only depends on the partial molar enthalpy changing with x but also the concentration of the ions within the electrode [Eq.(6)]. Therefore, to further investigate the effect of enthalpy of mixing, energy balance calculation was carried on in the next subsection.

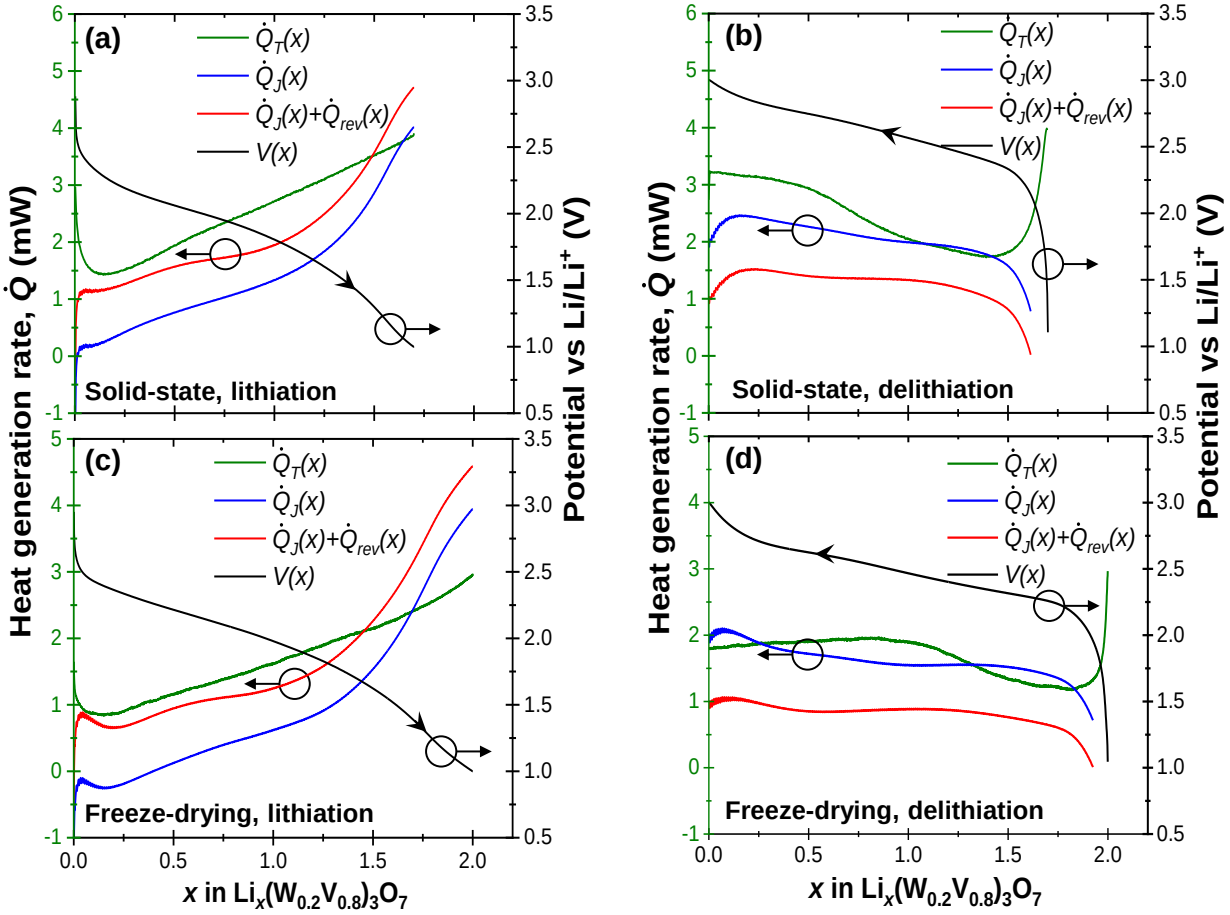

Figure 6: Measured total heat generation rate $\dot{Q}_T$=$\dot{Q}_{Li}$+$\dot{Q}_{WVO}$ and calculated heat generation rates $\dot{Q}_J$ and $\dot{Q}_J$+$\dot{Q}_{rev}$ calculated according to Eqs.(4) and (5) along with the measured voltage $V(x)$ upon (a) lithiation, (b) delithiation at C-rate of 3C for a cell containing electrode consisted of $(W_{0.2}V_{0.8})_3O_7$ microparticles synthesized by solid-state method, and (c) lithiation, (d) delithiation for a cell containing electrode consisted of $(W_{0.2}V_{0.8})_3O_7$ nanoparticles synthesized by freeze-drying method at temperature $T = 20$ °C.

4.3.4 Energy balance

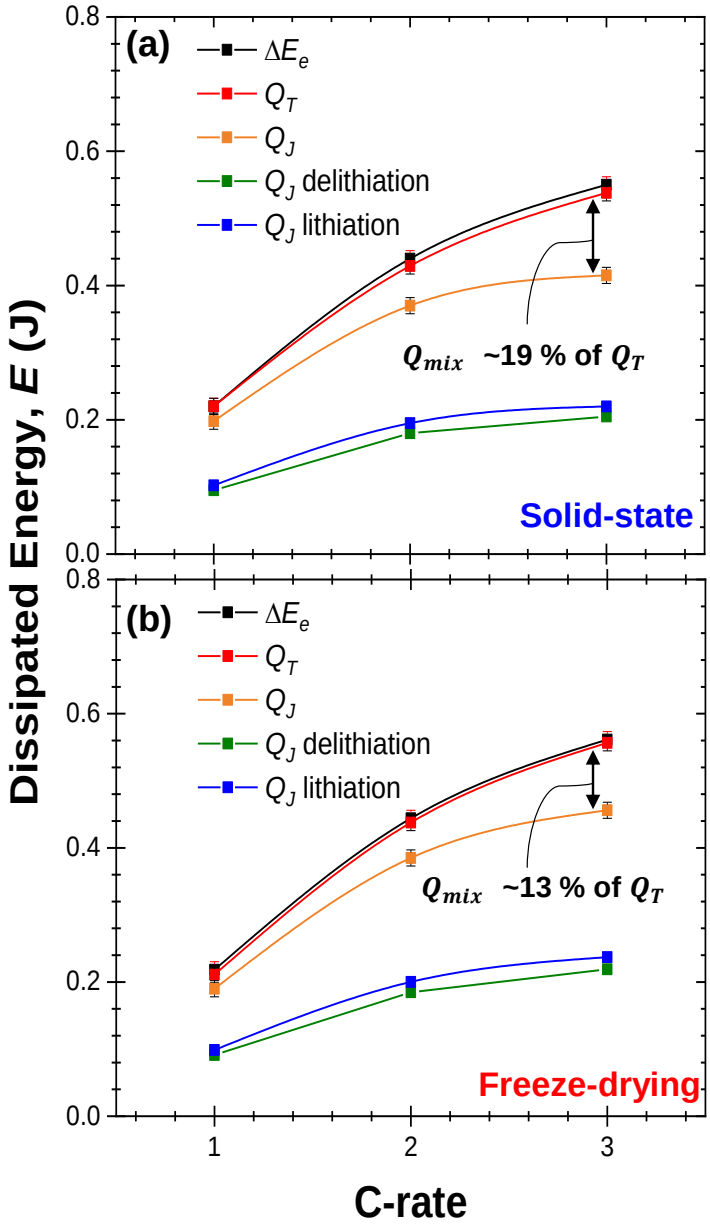

Figure 7: Net electrical energy losses ΔE_e and total thermal energy dissipated Q_T averaged over the first five charging-discharging cycles as well as contributions from Joule heating Q_J during lithiation and delithiation for a cell containing electrode consisted of $W_{0.2}V_{0.8})_3O_7$ (a) microparticles synthesized by solid-state method, and (b) nanoparticles synthesized by freeze-drying method. The enthalpy of mixing corresponds to $Q_{mix} = Q_T - Q_J = \Delta E_e - Q_J$.

Figures 7(a) and 7(b) presents the electrical energy losses ΔE_e measured from the hysteric voltage profile [Eq.(9)] along with the contributions from Joule heating Q_J [Eq.(8)] as well as the total thermal energy Q_T dissipated in the entire cell containing electrodes made of $(W_{0.2}V_{0.8})_3O_7$ particles synthesized by solid-state and freeze-drying methods, respectively at C-rates of 1C, 2C, and 3C. Here, for both cells, ΔE_e increased with increasing C-rate due to the associated increase in the overpotential $[V(x,T) - U^{avg}(x,T)]$ [38,39]. Moreover, the electrical energy losses ΔE_e due to the hysteric voltage profile fell within 5 % of the measured total thermal energy Q_T dissipated over cycle. In other words, the electrical energy losses were dissipated in the form of heat so that $\Delta E_e = Q_T$. In addition, the calculated Joule heating during delithiation was smaller than that during lithiation due to relatively fast kinetics of delithiation compared to that of lithiation as observed in the apparent diffusion coefficient of Li^+ ion in the $(W_{0.2}V_{0.8})_3O_7$ electrode (see Supplementary Material). Moreover, since $Q_{rev} \simeq 0$, the difference between Q_T and Q_J corresponded to the heat dissipated in the form of enthalpy of mixing, i.e., Q_{mix}=Q_T - Q_J. For a cell containing electrode consisted of $(W_{0.2}V_{0.8})_3O_7$ microparticles synthesized by solid-state method, the contribution of the enthalpy of mixing to the total energy dissipated increased with increasing C-rate to reach 19 % at C-rate of 3C. On the other hand, for a cell containing electrode consisted of $(W_{0.2}V_{0.8})_3O_7$ nanoparticles, the contribution of the enthalpy of mixing to the total energy dissipated was 13 % at C-rate of 3C. The present results suggest that the contribution of the enthalpy of mixing in the heat generation increased with increasing C-rate, and the contribution of the enthalpy of mixing was larger for the electrode made of microparticles synthesized by solid-state method than that of nanoparticles synthesized by freeze-drying method. These new calorimetry measurements confirmed that the smaller particle size was kinetically more advantageous for lithium-ions to intercalate than the larger particle size and resulted in smaller Joule heating as well as enthalpy of mixing.

5 Conclusion

This study investigated the effect of particle size of $(W_{0.2}V_{0.8})_3O_7$ on not only the electrochemical performances but also the thermodynamic properties as well as the associated heat generation. The cyclic voltammetry and galvanostatic cycling confirmed that the electrode consisted of $(W_{0.2}V_{0.8})_3O_7$ nanoparticle synthesized by the freeze-drying method showed superior electrochemical performances over that of the $(W_{0.2}V_{0.8})_3O_7$ microparticle synthesized by solid-state method. The entropic potential measurements not only confirmed the phase transition identified from XRD measurements but also identified increase in charge transfer resistance observed with potentiostatic electrochemical impedance spectroscopy. Furthermore, entropic potential measurements demonstrated that the $(W_{0.2}V_{0.8})_3O_7$ nanoparticle suppressed two-phase coexistence region. The isothermal *operando* calorimetry measurements demonstrated that the heat generation rate increased at the $(W_{0.2}V_{0.8})_3O_7$-based electrode upon lithiation due to increase in charge transfer resistance. Furthermore, calorimetric measurements established that the entropy change dominated the reversible heat generation rate at each electrode. Moreover, the time-averaged irreversible heat generation rate showed that the electrode made of nanoparticles was electrically less resistive resulting in less Joule heating compared to that of microparticles. Finally the contribution of enthalpy of mixing was smaller for $(W_{0.2}V_{0.8})_3O_7$ nanoparticles than that of microparticles confirming that smaller particle size was kinetically more advantageous for lithium-ions to intercalate into the active material.

6 Acknowledgment

This work was supported as part of the Center for Synthetic Control Across Length-scales for Advancing Rechargeables (SCALAR), an Energy Frontier Research Center funded by the U.S. Department of Energy, Office of Science, Basic Energy Sciences under Award # DE-SC0019381. The MRL Shared Experimental Facilities are supported by the MRSEC Program of the NSF under Award No. DMR 1720256; a member of the NSF-funded Materials

Research Facilities Network (www.mrfn.org).

References

[1] K. Mizushima, P. C. Jones, P. J. Wiseman, and J. B. Goodenough, "Li_xCoO_2 (0<x<-1): A new cathode material for batteries of high energy density," *Materials Research Bulletin*, vol. 15, no. 6, pp. 783 – 789, 1980.

[2] L.-X. Yuan, Z.-H. Wang, W.-X. Zhang, X.-L. Hu, J.-T. Chen, Y.-H. Huang, and J. B. Goodenough, "Development and challenges of $LiFePO_4$ cathode material for lithium-ion batteries," *Energy & Environmental Science*, vol. 4, no. 2, pp. 269–284, 2011.

[3] S. Lee, Y. Oshima, E. Hosono, H. Zhou, K. Kim, H. M. Chang, R. Kanno, and K. Takayanagi, "Phase transitions in a $LiMn_2O_4$ nanowire battery observed by operando electron microscopy," *ACS Nano*, vol. 9, no. 1, pp. 626–632, 2015.

[4] Y. Liu, Y. Zhu, and Y. Cui, "Challenges and opportunities towards fast-charging battery materials," *Nature Energy*, vol. 4, no. 7, pp. 540–550, 2019.

[5] S. W. Baek, K. E. Wyckoff, D. M. Butts, J. Bienz, A. Likitchatchawankun, M. B. Preefer, M. Frajnkovič, B. S. Dunn, R. Seshadri, and L. Pilon, "*Operando* calorimetry informs the origin of rapid rate performance in microwave-prepared $TiNb_2O_7$ electrodes," *Journal of Power Sources*, vol. 490, p. 229537, 2021.

[6] R. S. Roth, A. D. Wadsley, and S. Andersson, "The crystal structure of PNb_9O_{25}," *Acta Crystallographica*, vol. 18, no. 4, pp. 643–647, 1965.

[7] X. Zhu, J. Xu, Y. Luo, Q. Fu, G. Liang, L. Luo, Y. Chen, C. Lin, and X. S. Zhao, "$MoNb_{12}O_{33}$ as a new anode material for high-capacity, safe, rapid and durable Li^+ storage: structural characteristics, electrochemical properties and working mechanisms," *Journal of Material Chemistry A*, vol. 7, pp. 6522–6532, 2019.

[8] K. J. Griffith, I. D. Seymour, M. A. Hope, M. M. Butala, L. K. Lamontagne, M. B. Preefer, C. P. Kocer, G. Henkelman, A. J. Morris, and M. J. Cliffe, "Ionic and electronic conduction in $TiNb_2O_7$," *Journal of the American Chemical Society*, vol. 141, no. 42, pp. 16 706–16 725, 2019.

[9] M. B. Preefer, M. Saber, Q. Wei, N. H. Bashian, J. D. Bocarsly, W. Zhang, G. Lee, J. Milam-Guerrero, E. S. Howard, R. C. Vincent, B. C. Melot, A. Van der Ven, R. Seshadri, and B. S. Dunn, "Multielectron redox and insulator-to-metal transition upon lithium insertion in the fast-charging, Wadsley-Roth phase PNb_9O_{25}," *Chemistry of Materials*, vol. 32, no. 11, pp. 4553–4563, 2020.

[10] K. E. Wyckoff, D. D. Robertson, M. B. Preefer, S. M. Teicher, J. Bienz, L. Kautzsch, T. E. Mates, J. A. Cooley, S. H. Tolbert, and R. Seshadri, "High-capacity Li^+ storage through multielectron redox in the fast-charging wadsley–roth phase $(W_{0.2}V_{0.8})_3O_7$," *Chemistry of Materials*, vol. 32, no. 21, pp. 9415–9424, 2020.

[11] K. Nagata, H. Iwabuki, and H. Nigo, "Effect of particle size of graphites on electrical conductivity of graphite/polymer composite," *Composite interfaces*, vol. 6, no. 5, pp. 483–495, 1998.

[12] D.-H. Kim and J. Kim, "Synthesis of $LiFePO_4$ nanoparticles in polyol medium and their electrochemical properties," *Electrochemical and Solid-State Letters*, vol. 9, no. 9, pp. A439–A442, 2006.

[13] Z. Yang, D. Choi, S. Kerisit, K. M. Rosso, D. Wang, J. Zhang, G. Graff, and J. Liu, "Nanostructures and lithium electrochemical reactivity of lithium titanites and titanium oxides: A review," *Journal of Power Sources*, vol. 192, no. 2, pp. 588–598, 2009.

[14] O. Munteshari, J. Lau, A. Krishnan, B. S. Dunn, and L. Pilon, "Isothermal calorimeter for measurements of time-dependent heat generation rate in individual supercapacitor electrodes," *Journal of Power Sources*, vol. 374, pp. 257–268, 2018.

[15] A. Van der Ven, J. Bhattacharya, and A. A. Belak, "Understanding Li diffusion in Li-intercalation compounds," *Accounts of Chemical Research*, vol. 46, no. 5, pp. 1216–1225, 2013.

[16] S. W. Baek, M. B. Preefer, M. Saber, K. Zhai, M. Frajnkovič, Y. Zhou, B. S. Dunn, A. Van der Ven, R. Seshadri, and L. Pilon, "Potentiometric entropy and *operando* calorimetric measurements reveal fast charging mechanisms in PNb_9O_{25}," *Journal of Power Sources*, vol. 520, p. 230776, 2022.

[17] M. Chase, *NIST-JANAF Thermochemical Tables, 4th Edition.* New York, NY, USA: American Institute of Physics, 1998.

[18] Y. Wang, K. Zaghib, A. Guerfi, F. Bazito, R. Torresi, and J. Dahn, "Accelerating rate calorimetry studies of the reactions between ionic liquids and charged lithium ion battery electrode materials," *Electrochimica Acta*, vol. 52, no. 22, pp. 6346–6352, 2007.

[19] X. Feng, M. Fang, X. He, M. Ouyang, L. Lu, H. Wang, and M. Zhang, "Thermal runaway features of large format prismatic lithium ion battery using extended volume accelerating rate calorimetry," *Journal of Power Sources*, vol. 255, pp. 294–301, 2014.

[20] H. Giel, D. Henriques, G. Bourne, and T. Markus, "Investigation of the heat generation of a commercial 2032 ($LiCoO_2$) coin cell with a novel differential scanning battery calorimeter," *Journal of Power Sources*, vol. 390, pp. 116–126, 2018.

[21] A. Du Pasquier, F. Disma, T. Bowmer, A. Gozdz, G. Amatucci, and J.-M. Tarascon, "Differential scanning calorimetry study of the reactivity of carbon anodes in plastic Li-ion batteries," *Journal of the Electrochemical Society*, vol. 145, no. 2, pp. 472–477, 1998.

[22] G. Assat, S. L. Glazier, C. Delacourt, and J.-M. Tarascon, "Probing the thermal effects of voltage hysteresis in anionic redox-based lithium-rich cathodes using isothermal calorimetry," *Nature Energy*, vol. 4, no. 8, pp. 647–656, 2019.

[23] A. Likitchatchawankun, G. Whang, J. Lau, O. Munteshari, B. S. Dunn, and L. Pilon, "Effect of temperature on irreversible and reversible heat generation rates in ionic liquid-based electric double layer capacitors," *Electrochimica Acta*, vol. 338, p. 135802, 2020.

[24] O. Munteshari, A. Borenstein, R. H. DeBlock, J. Lau, G. Whang, Y. Zhou, A. Likitchatchawankun, R. B. Kaner, B. Dunn, and L. Pilon, "*In operando calorimetric measurements for activated carbon electrodes in ionic liquid electrolytes under* −1026, 2020.

[25] A. Likitchatchawankun, A. Kundu, O. Munteshari, T. S. Fisher, and L. Pilon, "Heat generation in all-solid-state supercapacitors with graphene electrodes and gel electrolytes," *Electrochimica Acta*, vol. 303, pp. 341–353, 2019.

[26] O. Munteshari, J. Lau, A. Likitchatchawankun, B.-A. Mei, C. S. Choi, D. Butts, B. S. Dunn, and L. Pilon, "Thermal signature of ion intercalation and surface redox reactions mechanisms in model pseudocapacitive electrodes," *Electrochimica Acta*, vol. 307, pp. 512–524, 2019.

[27] A. Likitchatchawankun, R. H. DeBlock, G. Whang, O. Munteshari, M. Frajnkovič, B. S. Dunn, and L. Pilon, "Heat generation in electric double layer capacitors with neat and diluted ionic liquid electrolytes under large potential window between 5 and 80 °C," *Journal of Power Sources*, vol. 488, p. 229368, 2021.

[28] O. Munteshari, J. Lau, D. S. Ashby, B. S. Dunn, and L. Pilon, "Effects of constituent materials on heat generation in individual EDLC electrodes," *Journal of The Electrochemical Society*, vol. 165, no. 7, p. A1547, 2018.

[29] G. Liu, M. Ouyang, L. Lu, J. Li, and X. Han, "Analysis of the heat generation of lithium-ion battery during charging and discharging considering different influencing factors," *Journal of Thermal Analysis and Calorimetry*, vol. 116, no. 2, pp. 1001–1010, 2014.

[30] J. Newman, K. E. Thomas, H. Hafezi, and D. R. Wheeler, "Modeling of lithium-ion batteries," *Journal of Power Sources*, vol. 119, pp. 838–843, 2003.

[31] K. E. Thomas and J. Newman, "Thermal modeling of porous insertion electrodes," *Journal of The Electrochemical Society*, vol. 150, no. 2, p. A176, 2003.

[32] W. Lu and J. Prakash, "*In situ* measurements of heat generation in a Li/mesocarbon microbead half-cell," *Journal of the Electrochemical Society*, vol. 150, no. 3, p. A262, 2003.

[33] K. Thomas and J. Newman, "Heats of mixing and of entropy in porous insertion electrodes," *Journal of Power Sources*, vol. 119, pp. 844–849, 2003.

[34] K. Smith and C.-Y. Wang, "Power and thermal characterization of a lithium-ion battery pack for hybrid-electric vehicles," *Journal of Power Sources*, vol. 160, no. 1, pp. 662–673, 2006.

[35] G. Heurung and R. Gruehn, "High-resolution transmission electron microscopy—investigation of vanadium-tungsten oxides prepared by chemical transport reactions," *Journal of Solid State Chemistry*, vol. 55, no. 3, pp. 337–343, 1984.

[36] T. Kim, W. Choi, H.-C. Shin, J.-Y. Choi, J. Kim, M.-S. Park, and W.-S. Yoon, "Applications of voltammetry in lithium ion battery research," *Journal of Electrochemical Science and Technology*, vol. 11, no. 1, pp. 14–25, 2020.

[37] J. B. Cook, T. C. Lin, H.-S. Kim, A. Siordia, B. S. Dunn, and S. H. Tolbert, "Suppression of electrochemically driven phase transitions in nanostructured MoS_2 pseudocapacitors probed using operando X-ray diffraction," *ACS nano*, vol. 13, no. 2, pp. 1223–1231, 2019.

[38] M. Ecker, J. B. Gerschler, J. Vogel, S. Käbitz, F. Hust, P. Dechent, and D. U. Sauer, "Development of a lifetime prediction model for lithium-ion batteries based on extended accelerated aging test data," *Journal of Power Sources*, vol. 215, pp. 248–257, 2012.

[39] D. Andre, M. Meiler, K. Steiner, C. Wimmer, T. Soczka-Guth, and D. U. Sauer, "Characterization of high-power lithium-ion batteries by electrochemical impedance spectroscopy. I. experimental investigation," *Journal of Power Sources*, vol. 196, no. 12, pp. 5334–5341, 2011.